SIMULTANEOUS IMPROVEMENT OF RESOLUTION AND ACCURACY OF 3D MAPPING WITH FLASH LIDAR THROUGH AI-BASED DATA FUSION WITH 2D CAMERA IMAGES

A. Liesch*, P. Suwinski*, V. Chernykh*, K. Janschek*

* Institute of Automation, Faculty of Electrical and Computer Engineering, TUD Dresden University of Technology, 01187 Dresden, Germany

Abstract

For the future exploration of our solar system, missions to Small Solar System Bodies (SSSBs), such as asteroids or comets, are a promising and scientifically important area. For navigation and guidance tasks, high-resolution and high-accuracy 3D distance maps of the surface are required. Flash-LiDAR sensors are often used to capture the surface of a SSSB, but they are limited in resolution. This paper proposes an artificial intelligence (AI) based approach to simultaneously improve the resolution and accuracy of 3D distance maps generated by flash-LiDAR through AI-based data fusion with 2D camera images. Our method leverages the smaller ground sampling distance (GSD) of the 2D camera images and the distinct error behavior of 3D surface reconstruction from LiDAR and camera data. A generative adversarial network (GAN) architecture was designed for that purpose. We evaluated our approach extensively with a custom generated synthetically dataset of an asteroid surface. As a result of the tests, a simultaneous improvement of the ground resolution by a factor of 4×4 and suppression of the RMSE distance error by a factor of 1.31 with respect to the simulated flash-LiDAR data was successfully demonstrated.

Keywords Artificial Intelligence; Guidance, Navigation and Control; Space Exploration

NOMENCLATURE

Abbreviations

ΑŢ

111	Ti diliciai intenigence
CNN	Convolutional Neural Network
DEM	Digital Elevation Map
DN	Discrimantor Network
GAN	Generative Adversarial Network
GN	Generator Network
GSD	Ground Sampling Distance
LiDAR	Light imaging, detection and ranging
MSE	Mean Squared Error
NN	Neural Network
PNSR	Peak Signal to Noise Ratio
RMSE	Root Mean Squared Error
SfS	Shape from Shading
SSSB	Small Solar System Body

Artificial Intelligence

1. INTRODUCTION

Missions to SSSBs, such as asteroids or comets, are a promising and scientifically important area for future solar system exploration. Exploring asteroids or comets can provide valuable insights into the genesis and progression of our solar system while also enabling us to identify lucrative resources for upcoming space missions. However, these exploration missions pose numerous challenges. Besides the small, varying gravity or the unstructured, irregular surface and landform, the long distances to Earth, particularly the impossible real-time communication between ground control and the exploring spacecraft, is one major problem. Current missions to the close vicinity of SSSBs require plenty of human monitoring and processing to ensure a safe flight. Thus, the exploration of SSSBs is intrinsically tied to the achievement of autonomy within mission operations.

Recent space missions have been incorporating increasingly advanced technologies to overcome the limitations of human involvement. Hayabusa-2 [1], launched in 2014, utilized upgraded navigation tools and advanced characterization techniques such as radiometric tracking and autonomous descent. OSIRIS-REx [2], launched in 2016, took it a step further by incorporating vision-based navigation for close-range operations, advanced exposure techniques,

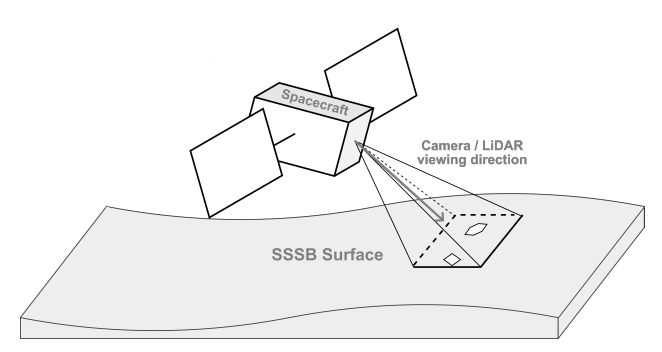


FIG 1. Concept of Astrone and Astrone KI's navigation system

and landmark tracking in addition to radiometric tracking. Most recently, DART [3] launched successfully in 2021 and achieved kinetic impact deflection using a fully autonomous navigation system and avionics.

As part of the Astrone [4, 5] project, a flash-LiDAR-augmented inertial navigation system has been developed. This system enables advanced surface mobility for science and exploration operations on the surfaces of SSSBs like the comet 67P/Churyumov-Gerasimenko. The system uses 3D distance maps generated by flash-LiDAR to update the navigation filter and generate 3D maps of the SSSB's surface. Fig. 1 depicts the conceptual pro-In the follow-up project, Astrone KI, an AI-based approach to increase the resolution of a 3D distance map by data fusion with a single monocular 2D greyscale image, both taken from wide-angle optics, was proposed and successfully tested in a simulation environment [6]. The higher-resolution 3D distance map enables implementing other AI-based systems for Astrone KI's navigation concept [7, 8]. A high-resolution monocular grayscale camera with a resolution of 1024×1024 pixels and a flash-LiDAR provides a resolution of 256×256 provide the needed data.

To further improve the navigation system's performance, we present an approach to simultaneously improving the resolution and accuracy of 3D distance maps through AI-based data fusion with 2D camera images. We investigate the algorithms' behavior in relation to noisy flash-LiDAR data. The goal was to develop an algorithm without relying on multiple neural networks for different subtasks of the data fusion.

To this end, our main contributions are:

- Improve the resolution and accuracy of 3D distance maps through AI-based data fusion with 2D camera images.
- 2) The neural network training and test campaign results in the simulated asteroid environment.

2. RELATED WORK

Flash-LiDAR utilizes a time-of-flight method to measure distances, resulting in minimal distance-dependent errors. For each pixel, the absolute distance is determined individually. As a result, it has the advantage of no pixel-to-pixel dependency and error accumulation across the frame. On the other hand, a flash-LiDAR is limited in resolution, and measurements have a relatively large distance error. Especially for small distances, in the context of space exploration, a few meters can cause distance errors to exceed the GSD.

Analytical methods like Shape-from-Shading (SfS) [9] can provide high-resolution data and a low local error to compensate for some of flash-LiDAR's disadvantages. SfS extracts local gradients from 2D image data and then integrates the gradients to reconstruct the 3D surface. This results in a high-resolution 3D image with small local distance errors. While Gaskell et al. (2008) [10] and Al Asad et al. (2021) [11] have used a SfS approach in the context of an asteroid surface, there are limitations such as scale ambiguity, distance error accumulation across the field of view, and the need to capture multiple images of the same scene under different illumination conditions, making it challenging to apply to the context of an asteroid surface.

In recent years, different machine learning approaches, such as artificial neural networks (NN), achieved game-changing results in computer vision tasks such as classification, segmentation, super-resolution, and 3D reconstruction. Especially for 3D reconstruction, monocular depth estimation, depth super-resolution, or depth completion have become active research fields with many, but mainly for terrestrial applica-The approaches used in these fields, which rely on deep neural networks, can be categorized by their fusion strategies. These methods are early, late, and hybrid. Each fusion method has its advantages and disadvantages. Early fusion easily identifies the relationships between features but often leads to overfitting. On the other hand, late fusion can address overfitting issues, but it does not allow the classifier to train on all the data simultaneously. Hybrid fusion, however, offers more flexibility than the previous two methods. Nevertheless, it requires selecting suitable fusion approaches based on the specific architecture, problems, and research topic. [12, 13]

Usually, an encoder-decoder network is utilized to first encode different input signals into a common latent space, enabling feature fusion. Then, a decoder reconstructs an output depth map [14, 15]. With AI-based methods, noisy input data remains a challenge. To address this issue, FusionNet [16] fuses local and global information with a confidence map. Instead, PENet [17] fuses the output of a color-dominant branch and a depth-dominant branch, using a confidence map utilizing the benefits of a late fusion approach. Also, a

CycleGAN [18] approach was applied to synthetic and noisy LiDAR data for a sparse-to-dense completion. Most modern approaches are used in terrestrial applications. Many Datasets like KITTI [19, 20], SYN-THIA [21], or NYUv2 [22] are available in this context for training and testing. On the other hand, the surface of celestial bodies or small solar system bodies can vary significantly. Different illumination conditions and an unstructured surface differ greatly from typical applications. Usable, realistic datasets are often closed-source or do not exist. One exception is the Artificial Lunar Landscape [23], which lacks necessary LiDAR data. Despite that, AI-based methods were applied to environments comparable to the surface of an SSSB: The Mars3Dnet13 [24] used a Convolutional Neural Network (CNN)-based structure to predict a high-resolution Digital Elevation Model (DEM) from one monocular grayscale 2D image and subsequently fused this with a low-resolution DEM. Synthetic and real data, including context camera images of the Martian surface, were used for training. Another CNNbased approach was given by Chen et al. (2022) [25], where a high-resolution image and a low-resolution DEM of the lunar surface were used to predict a highresolution DEM. Then, SfS was applied to improve details. Also, GAN-based approaches have demonstrated effectiveness under these conditions in recent works [26, 27, 28].

Liesch et al. (2023) [6] presented a solution to combine the advantages of flash-LiDAR and SfS in the context of asteroid exploration missions. This GAN-based solution provides high-resolution data and generally suppresses scale ambiguity and distance error accumulation for small local residuals, but the LiDAR distance error was not corrected.

3. CONCEPT

3.1. Overview

Fig. 2 illustrates the processing pipeline. Our approach employs a low-resolution depth image with normally distributed noise and a high-resolution grayscale camera image as guidance. Both input sources are assumed to be perfectly calibrated. The general idea is to extract high-frequency components from the camera image and low frequencies from the depth image. The performance of neural networks is highly dependent on the quality and characteristics of the training data. To enhance robustness against noisy inputs and to promote the generation of higher-resolution and more accurate outputs, the neural network was trained using data intentionally augmented with noise.

3.2. Principle of the distance noise suppression

Distance noise reduction due to data fusion is possible due to the different behavior of LiDAR and SfS errors. With flash-LiDAR, the absolute local distance is determined independently for each pixel of the array. The error occurs in the time domain (time-of-flight

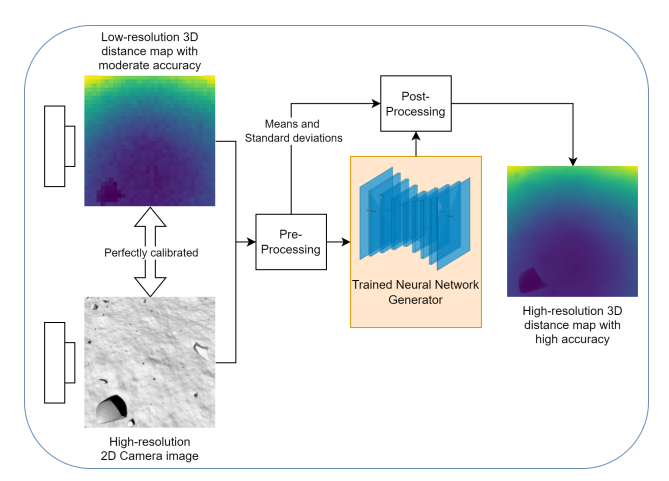


FIG 2. Concept and camera-LiDAR set-up

measurement) and has a low dependence on the target distance within the operating range. As a result, for moderate distances and large flash-LiDAR arrays (Astrone KI's application case), the σ_1 distance error of the distribution can be larger than the GSD. For SfS, the relative local distance is determined by integrating local slopes (gradients). In this case, the distance difference between adjacent pixels can be determined with an error generally well below the GSD, but the error rapidly grows with increasing sampling interval. Fig. 3 shows an example of the distance error suppression for the simplified error model (zero mean Gaussian noise) and distance values typical for Astrone KI's application scenario.

Fig. 3a shows an example of LiDAR data: absolute distances with correct scaling for each pixel of the flash-LiDAR. At the same time, the distance error is relatively high ($\sigma_1 = 0.05 \,\mathrm{m}$, which even exceeds the $GSD(0.04 \,\mathrm{m})$). The error can be greatly reduced by averaging 5×5 pixels at the cost of losing small details (Fig. 3b). The SfS data (Fig. 3c) are relative (no absolute values) and scaled only with respect to the GSD. In this case, the errors are much smaller (σ well below the GSD), especially for the pixels close to the center of the processed area. Finally, Fig. 3d shows the result of the fusion of the averaged LiDAR data (Fig. 3b) and the SfS data (Fig. 3c): with respect to the LiDAR data (Fig. 3a), absolute distance values, correct scaling and small details are preserved, while the errors are significantly reduced.

Since the real error behavior differs from the idealized Gaussian distribution, an AI-based solution was applied to deal with the complicated error models.

3.3. Design of the Neural Network

3

Our neural network builds on an advanced GAN framework proposed by Liesch et al. (2023) [6], designed to enhance the resolution of the 3D distance map and reconstruct high-frequency surface components. The GAN architecture comprises a generator network (GN) and a discriminator network (DN), which are trained in a competitive manner.

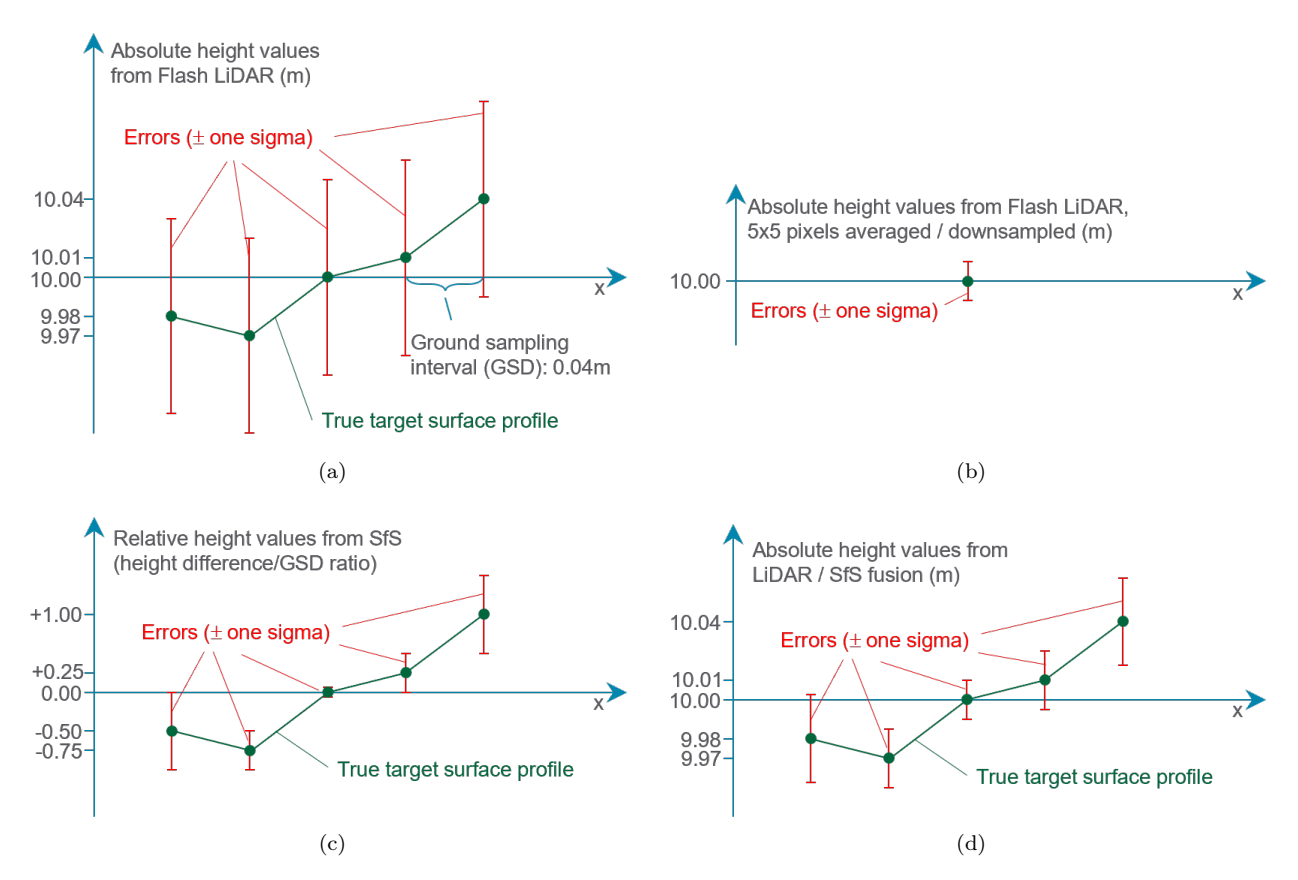


FIG 3. Error reduction as a result of the flash-LiDAR / SfS data fusion. x represents the samples in the image plane.

Accordingly, the GAN loss is used, defined by the functions D and G, representing the DN and GN, respectively:

$$\mathcal{L}_{GAN}(G, D) = \mathbb{E}_{\mathbf{y}}[\log_e D(\mathbf{y})] + \mathbb{E}_{\mathbf{I}_{LR}, \mathbf{I}_{HR}}[\log_e (1 - D(G(\mathbf{I}_{LR}, \mathbf{I}_{HR})))]$$
(1)

Additionally, Isola et al. (2018) [29] suggested using the L1 distance, which encourages less blurring than the L_2 distance. L_1 will force low-frequency correctness. Although this will fail to capture details and high frequencies, the discriminator network will take care of this:

$$\mathcal{L}_{L1}(G) = \mathbb{E}_{\mathbf{y}, \mathbf{I}_{LR}, \mathbf{I}_{HR}}[\mathbf{y} - G(\mathbf{I}_{LR}, \mathbf{I}_{HR})]$$
 (2)

The combined loss function L incorporates both \mathcal{L}_{GAN} and \mathcal{L}_{L1} , with the hyperparameter λ controlling the influence of \mathcal{L}_{L1} . In our implementation, we set $\lambda = 100$

$$G^* = \arg\min_{G} \max_{D} \mathcal{L}_{GAN}(G, D) + \lambda \mathcal{L}_{L1}(G)$$
 (3)

3.4. Data Pre- and Postprocessing Procedures

Due to GPU memory constraints, the input camera image and low-resolution 3D distance map are divided into smaller patches and processed individually by the

GN. The GAN architecture requires that the input data be rescaled between 0 and 1. This requirement is derived from Eq. 1, where the binary cross entropy loss function is used to calculate \mathcal{L}_{GAN} . A min/max normalization brings the data to the required form. The mean and standard derivation are calculated per input distance image patch to recover the original scaling with absolute values later in the postprocessing after the processing by the GN. The final preprocessing step resizes the low-resolution input patches to the same size as the camera image patches. Missing values are set to 0. That step allows concatenating both inputs to $128 \times 128 \times 2$ per tile. Now all resulting 64 tiles, for an input resolution of 1024×1024 , have the correct form to be passed to the GN in parallel.

Accordingly, the output of the GN contains 64 patches with a size of 128×128 . The means and standard deviations obtained during the preprocessing are used to recover the original scale and absolute values. As the final step of postprocessing, all patches are combined to create a complete high-resolution and accurate 3D distance map with absolute values.

4. EXPERIMENTS

4.1. Dataset generation

To address the scarcity of publicly available datasets and adhere to the specifications of the Astrone KI project, we developed a custom dataset us-

ing the project's data generation tool. A virtual spacecraft, designed with specifications closely resembling those of the anticipated real spacecraft, was employed in the simulation. This virtual spacecraft navigated the simulated surface of comet 67P/Churyumov-Gerasimenko along various trajectories, mimicking the jump-like movements expected of the real spacecraft. During these simulated trajectories, high-resolution images (1024×1024 pixels) and corresponding depth images were captured using a virtual camera and flash-LiDAR sensor for a large Field of View of $65^{\circ} \times 65^{\circ}$. Both sensors were perfectly calibrated and aligned according to project requirements. The nadir angle has been changed between 0° and 50° to cover a wider range of scenarios during a mission. Following the initial data generation, the high-resolution depth images were downsampled to obtain low-resolution depth images, in line with the project's investigation needs. Additionally, normally distributed noise was added to the low-resolution depth images to further simulate inaccurate LiDAR measurement and more realistic conditions in this preliminary analysis. In total, about 10,000 individual samples have been created.

4.2. Training specifications and evaluation metrics

We trained the GAN using our specifically created dataset. We employed low-resolution depth images with noise and camera image pairs. For the training process, 7000 samples were used. The training was conducted using Adams optimizers with $\beta_1=0.9$ and $\beta_2=0.999$ and a learning rate of 10^{-7} for the generator and discriminator network on a single NVIDIA RTX 3090 GPU and an AMD Ryzen 5950x CPU. Both networks were efficiently trained using the AI framework Tensorflow [30] for 30 epochs.

After the training, the generator network's performance was evaluated quantitatively using the Peak Signal-to-Noise Ratio (PSNR), Mean average error (MAE), Root Mean Squared Error (RMSE), Mean Squared Error (MAE), and qualitatively using visual comparisons. The metrics can be computed between the output \mathbf{y} and ground truth depth image $\hat{\mathbf{y}}$ according to Eq. 4a-4d using the total number of points per image n.

$$MAE = \frac{1}{n} \cdot \sum_{k=1}^{n} |\hat{\mathbf{y}}_k - \mathbf{y}_k|$$
 (4a)

$$MSE = \frac{1}{n} \cdot \sum_{k=1}^{n} |\hat{\mathbf{y}} - \mathbf{y}|^2$$
 (4b)

$$RMSE = \sqrt{\frac{1}{n} \cdot \sum_{k=1}^{n} |\hat{\mathbf{y}} - \mathbf{y}|^2}$$
 (4c)

$$PSNR = 20 \cdot \log_{10} \left(\frac{\mathbf{y}_{max}}{\sqrt{MSE}} \right)$$
 (4d)

A higher PSNR represents a more accurate reconstruction of the ground-truth image, where y_{max} is the maximum possible value of the depth image \mathbf{y} in Eq. 4d. Lower values are better for 4a-4c.

4.3. Results

In this section, we detail the experiments and results based on the network's architecture and overall concept, as discussed in Section 3. The quantitative performance, using the metrics explained in Section 4.2, is shown in Tab. 1 and 2. We utilized 2000 individual data samples from our custom-generated dataset that were not part of the training process for validation and testing purposes. The performance of our system was compared using a network trained with a standard approach (GN-standard) and a network trained specifically with noise (GN-noise). The system with the GN, specifically trained for noisy data, outperformed the system with the standard network. All metrics show a significant improvement compared to the standard approach. To verify the actual improvement in accuracy, we only compared the existing data points of the depth image before and after the processing. In other words, the low-resolution depth image was compared with the corresponding points of the highresolution output. Tab 2 shows that the GN, created without special training, could only increase the accuracy to a small amount. In the case of the MAE, the GN-standard creates an even worse result. However, GN-noise improved all metrics compared to the original input data and, therefore, improved the accuracy of the original measurements. The qualitative results

TAB 1. Quantitative comparison of different GNs in terms of the metrics defined in Eq. 4a-4d on our synthetically generated dataset. MAE, RMSE in cm, MSE in cm², and PSNR in db.

Version	MAE	MSE	RMSE	PSNR
GN-standard	4.06	40.91	6.39	25.67
GN-noise	2.09	26.00	5.09	31.18

are visually compared to ground truth for two scenes. Fig. 4 visually represents the input camera image, low-resolution LiDAR data, the output (GN-noise NN was used), and ground truth. Additionally, absolute errors are shown for the system's output and a simple bilinear upsampling of the low-resolution data. These results demonstrate the robustness of our algorithms against the noise. Recovering some high-resolution details from the input camera image and low-resolution depth image with $\sigma_1 = 5 \,\mathrm{cm}$ noise was possible. From the visualized absolute error, it is visible that the highest errors are around the edges of objects like stones. In comparison, the error on the surface is relatively small. However, large errors or effects of the noise applied to the low-resolution input data on the final output are not visible.

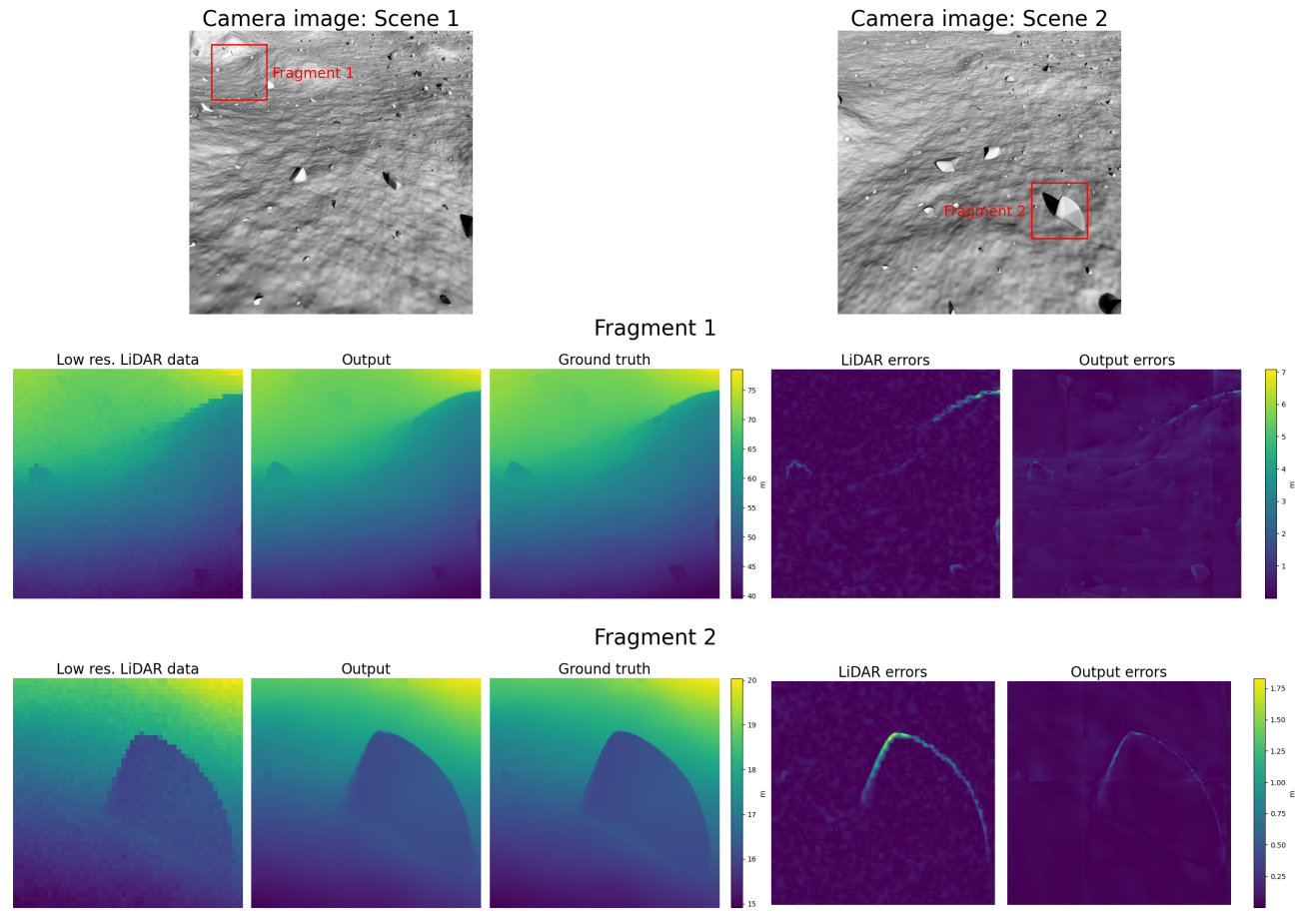


FIG 4. Qualtitative comparison of our system's output using the GN-noise NN to ground truth and bilinear upsampled low-resolution LiDAR data.

TAB 2. Quantitative comparison of already existing Li-DAR points before the processing and after the processing in terms of the metrics defined in Eq. 4a-4d on our synthetically generated dataset. MAE, RMSE in cm, MSE in cm², and PSNR in db.

Version	MAE	MSE	RMSE	PSNR
Before	3.99	25.00	5.00	26.02
GN-standard	4.36	34.26	5.85	25.26
GN-noise	2.07	14.64	3.82	31.58

5. CONCLUSION

An AI-based approach is proposed to simultaneously improve the resolution and accuracy of 3D distance maps generated by flash-LiDAR through AI-based data fusion with 2D camera images. The approach exploits the camera images' smaller ground sampling distance and the different error behavior of 3D surface reconstruction from LiDAR and camera data. A neural network was designed based on the advanced GAN framework. The network was trained with 7000 data samples (simulated camera and flash-LiDAR frames and ground truth data) from a custom dataset generated by a high-fidelity simulator of the asteroid surface. The trained network was tested with 2000

additional data samples (not used for training). As a result of the test, a simultaneous improvement of the ground resolution by a factor of 4×4 and suppression of the RMSE distance error by a factor of 1.31 with respect to the simulated flash-LiDAR data was successfully demonstrated.

6. ACKNOWLEDGEMENT

The project Astrone KI has received funding from the German Federal Ministry for Economic Affairs and Energy (BMWi) under funding number 50 RA 2130C supervised by the German Space Agency (DLR, Deutsches Zentrum für Luft- und Raumfahrt).

Contact address:

alexander.liesch@tu-dresden.de

References

- [1] Makoto Yoshikawa, Junichiro Kawaguchi, Akira Fujiwara, and Akira Tsuchiyama. "Hayabusa sample return mission". In: Asteroids IV 1.397-418 (2015), p. 1.
- [2] DS Lauretta et al. "OSIRIS-REx: sample return from asteroid (101955) Bennu". In: Space Science Reviews 212 (2017), pp. 925–984.

- [3] Patrick Michel et al. "European component of the AIDA mission to a binary asteroid: Characterization and interpretation of the impact of the DART mission". In: Advances in Space Research 62.8 (2018), pp. 2261–2272.
- [4] B. Liu, V. Sazdovski, V. Chernykh, et al. "Flash LiDAR Aided-Inertial Navigation on Surfaces of Small Solar System Bodies Using Error State Kalman Filtering". In: Paper AAS 21-752. AAS/AIAA Astrodynamics Specialist Conference. Aug 8-12, 2021.
- [5] M Martin et al. "Astrone–GNC for Enhanced Surface Mobility on Small Solar System Bodies". In: 11 th International ESA Conference on Guidance, Navigation & Control Systems. 2021.
- [6] A. Liesch, P. Suwinski, et al. "AI-based LiDAR / Camera data fusion to enable high-resolution 3D surface reconstruction for autonomous asteroid exploration mission". In: Paper AAS-422. AAS/AIAA Astrodynamics Specialist Conference, Big Sky, MT. Aug 13-17, 2023.
- [7] A. Liesch et al. "AI-based Mapping for Navigation on Significantly Unstructured Planetary Surfaces". In: Deutscher Luft-und Raumfahrt Kongress. Deutscher Luft- und Raumfahrt Kongress, Stuttgart, Germany. Sep 19-21, 2023. DOI: 10.25967/610423.
- [8] Patrick Suwinski, Alexander Liesch, Bangshang Liu, Valerij Chernykh, and Klaus Janschek. "AI-based Pre-Processing for Navigation on Significantly Unstructured Planetary Surfaces". In: Deutscher Luft- und Raumfahrt Kongress, Stuttgart, Germany. Sep 19-21, 2023. DOI: 10.25967/610427.
- [9] Berthold K. P. Horn. "Obtaining shape from shading information". In: Shape from Shading. Cambridge, MA, USA: MIT Press, 1989, pp. 123–171. ISBN: 0262081830.
- [10] R. W. Gaskell et al. "Characterizing and Navigating Small Bodies with Imaging Data". In: Meteoritics & Planetary Science 43.6 (2008), pp. 1049–1061. ISSN: 1945-5100. DOI: 10.1111/j.1945-5100.2008.tb00692.x.
- [11] M. M. Al Asad et al. "Validation of Stereophotoclinometric Shape Models of Asteroid (101955) Bennu during the OSIRIS-REx Mission". In: The Planetary Science Journal 2.2 (Apr. 29, 2021), p. 82. ISSN: 2632-3338. DOI: 10.3847/ PSJ/abe4dc. URL: https://iopscience.iop.org/ article/10.3847/PSJ/abe4dc/meta (visited on 06/26/2023).
- [12] Zexiao Xie, Xiaoxuan Yu, Xiang Gao, Kunqian Li, and Shuhan Shen. "Recent Advances in Conventional and Deep Learning-Based Depth Completion: A Survey". In: IEEE Transactions on Neural Networks and Learning Systems (2022), pp. 1–21. DOI: 10.1109/TNNLS.2022.3201534.

- [13] Jianghong Zhao et al. "The Fusion Strategy of 2D and 3D Information Based on Deep Learning: A Review". en. In: Remote Sensing 13.20 (Oct. 2021). Number: 20, p. 4029. ISSN: 2072-4292. DOI: 10.3390/rs13204029. URL: https://www.mdpi.com/2072-4292/13/20/4029 (visited on 07/13/2022).
- [14] Junjie Hu, Chenyu Bao, Mete Ozay, Chenyou Fan, Qing Gao, Honghai Liu, and Tin Lun Lam. Deep Depth Completion: A Survey. May 2022. DOI: 10.48550/arXiv.2205.05335. (Visited on 08/16/2022).
- [15] Zhihao Wang, Jian Chen, and Steven C. H. Hoi. "Deep Learning for Image Super-Resolution: A Survey". In: IEEE Transactions on Pattern Analysis and Machine Intelligence 43.10 (Oct. 2021). Number: 10 Conference Name: IEEE Transactions on Pattern Analysis and Machine Intelligence, pp. 3365–3387. ISSN: 1939-3539. DOI: 10.1109/TPAMI.2020.2982166.
- [16] Wouter Van Gansbeke, Davy Neven, Bert De Brabandere, and Luc Van Gool. "Sparse and Noisy LiDAR Completion with RGB Guidance and Uncertainty". In: 2019 16th International Conference on Machine Vision Applications (MVA). May 2019, pp. 1–6. DOI: 10.23919 / MVA.2019.8757939. URL: https://ieeexplore.ieee.org/document/8757939/?arnumber=8757939 (visited on 09/02/2024).
- [17] Mu Hu, Shuling Wang, Bin Li, Shiyu Ning, Li Fan, and Xiaojin Gong. PENet: Towards Precise and Efficient Image Guided Depth Completion. Mar. 18, 2021. DOI: 10.48550/arXiv.2103.00783. arXiv: 2103.00783 [cs].
- [18] Jun-Yan Zhu, Taesung Park, Phillip Isola, and Alexei A. Efros. Unpaired Image-to-Image Translation Using Cycle-Consistent Adversarial Networks. Aug. 24, 2020. DOI: 10.48550/arXiv.1703.10593. arXiv: 1703.10593 [cs]. (Visited on 09/02/2024).
- [19] Andreas Geiger, Philip Lenz, and Raquel Urtasun. "Are we ready for Autonomous Driving? The KITTI Vision Benchmark Suite". In: Conference on Computer Vision and Pattern Recognition (CVPR). 2012.
- [20] Andreas Geiger, Philip Lenz, Christoph Stiller, and Raquel Urtasun. "Vision meets Robotics: The KITTI Dataset". In: International Journal of Robotics Research (IJRR) (2013).
- 21] German Ros, Laura Sellart, Joanna Materzynska, David Vazquez, and Antonio M. Lopez. "The SYNTHIA Dataset: A Large Collection of Synthetic Images for Semantic Segmentation of Urban Scenes". In: 2016 IEEE Conference on Computer Vision and Pattern Recognition (CVPR). Las Vegas, NV, USA: IEEE, June 2016, pp. 3234–3243. ISBN: 978-1-4673-8851-1. DOI: 10.1109/CVPR.2016.352. URL:

CC BY-SA 4.0

7

- http://ieeexplore.ieee.org/document/7780721/(visited on 09/02/2024).
- [22] Camille Couprie, Clément Farabet, Laurent Najman, and Yann LeCun. Indoor Semantic Segmentation Using Depth Information. Mar. 14, 2013. arXiv: 1301.3572 [cs]. Pre-published.
- [23] Romain Pessia. Artificial Lunar Landscape Dataset. URL: https://www.kaggle.com/datasets/romainpessia/artificial-lunar-rocky-landscape-dataset (visited on 09/02/2024).
- [24] Zeyu Chen, Bo Wu, and Wai Chung Liu. "Mars3DNet: CNN-Based High-Resolution 3D Reconstruction of the Martian Surface from Single Images". In: Remote Sensing 13.5 (5 Jan. 2021), p. 839. DOI: 10.3390/rs13050839.
- [25] H. Chen, X. Hu, and J. Oberst. "PIXEL-RESOLUTION DTM GENERATION FOR THE LUNAR SURFACE BASED ON A COMBINED DEEP LEARNING AND SHAPE-FROM-SHADING (SFS) APPROACH". In: ISPRS Annals of the Photogrammetry, Remote Sensing and Spatial Information Sciences V-3-2022 (May 17, 2022), pp. 511–516. DOI: 10.5194/isprs-annals-V-3-2022-511-2022.
- [26] Yu Tao, Jan-Peter Muller, Siting Xiong, and Susan J. Conway. "MADNet 2.0: Pixel-Scale Topography Retrieval from Single-View Orbital Imagery of Mars Using Deep Learning". In: Remote Sensing 13.21 (21 Jan. 2021), p. 4220. ISSN: 2072-4292. DOI: 10.3390 / rs13214220. (Visited on 09/01/2022).
- [27] Yang Liu, Yexin Wang, Kaichang Di, Man Peng, Wenhui Wan, and Zhaoqin Liu. "A Generative Adversarial Network for Pixel-Scale Lunar DEM Generation from High-Resolution Monocular Imagery and Low-Resolution DEM". In: Remote Sensing 14.21 (21 Jan. 2022), p. 5420. ISSN: 2072-4292. DOI: 10.3390/rs14215420.
- [28] Riccardo La Grassa, Ignazio Gallo, Cristina Re, Gabriele Cremonese, Nicola Landro, Claudio Pernechele, Emanuele Simioni, and Mattia Gatti. "An Adversarial Generative Network Designed for High-Resolution Monocular Depth Estimation from 2D HiRISE Images of Mars". In: Remote Sensing 14.18 (18 Sept. 15, 2022), p. 4619. ISSN: 2072-4292. DOI: 10.3390/rs14184619.
- [29] Phillip Isola, Jun-Yan Zhu, Tinghui Zhou, and Alexei A. Efros. Image-to-Image Translation with Conditional Adversarial Networks. Nov. 2018. URL: http://arxiv.org/abs/1611.07004 (visited on 11/02/2022).
- [30] Martín Abadi et al. TensorFlow: Large-Scale Machine Learning on Heterogeneous Systems. Software available from tensorflow.org. 2015. URL: https://www.tensorflow.org/.